VIP Metal–Organic Frameworks Very Important Paper

How to cite: *Angew. Chem. Int. Ed.* **2022,** *61,* e202207259
International Edition: doi.org/10.1002/anie.202207259
German Edition: doi.org/10.1002/ange.202207259

Structural and Dynamic Analysis of Sulphur Dioxide Adsorption in a Series of Zirconium-Based Metal–Organic Frameworks

Jiangnan Li, Gemma L. Smith, Yinlin Chen, Yujie Ma, Meredydd Kippax-Jones, Mengtian Fan, Wanpeng Lu, Mark D. Frogley, Gianfelice Cinque, Sarah J. Day, Stephen P. Thompson, Yongqiang Cheng, Luke L. Daemen, Anibal J. Ramirez-Cuesta, Martin Schröder, and Sihai Yang**

Abstract: We report reversible high capacity adsorption of SO_2 in robust Zr-based metal–organic framework (MOF) materials. Zr-bptc (H_4bptc = biphenyl-3,3′,5,5′-tetracarboxylic acid) shows a high SO_2 uptake of 6.2 mmol g^{-1} at 0.1 bar and 298 K, reflecting excellent capture capability and removal of SO_2 at low concentration (2500 ppm). Dynamic breakthrough experiments confirm that the introduction of amine, atomically-dispersed Cu^{II} or heteroatomic sulphur sites into the pores enhance the capture of SO_2 at low concentrations. The captured SO_2 can be converted quantitatively to a pharmaceutical intermediate, aryl N-aminosulfonamide, thus converting waste to chemical values. In situ X-ray diffraction, infrared micro-spectroscopy and inelastic neutron scattering enable the visualisation of the binding domains of adsorbed SO_2 molecules and host–guest binding dynamics in these materials at the atomic level. Refinement of the pore environment plays a critical role in designing efficient sorbent materials.

[*] Dr. J. Li, Dr. G. L. Smith, Y. Chen, Y. Ma, M. Kippax-Jones, M. Fan, W. Lu, Prof. Dr. M. Schröder, Prof. Dr. S. Yang
Department of Chemistry, University of Manchester
Manchester, M13 9PL (UK)
E-mail: M.Schroder@manchester.ac.uk
sihai.yang@manchester.ac.uk

M. Kippax-Jones, Dr. M. D. Frogley, Dr. G. Cinque, Dr. S. J. Day, Dr. S. P. Thompson
Diamond of Light Source, Harwell Science Campus
Oxfordshire, OX11 0DE (UK)

Dr. G. Cinque
Department of Engineering Sciences, University of Oxford,
Oxford, OX1 3PJ (UK)

Dr. Y. Cheng, Dr. L. L. Daemen, Dr. A. J. Ramirez-Cuesta
Neutron Scattering Division, Oak Ridge National Laboratory
Oak Ridge, TN 37831 (USA)

Introduction

Sulphur dioxide (SO_2) is an important air pollutant as well as a key chemical feedstock for the synthesis of sulfuric acid and various fine chemicals.[1–5] State-of-the-art flue-gas desulphurisation (FGD) technology uses limestone slurry to capture SO_2 effectively, but this is an irreversible process that generates a tremendous amounts of solid waste.[6,7] Recovery of SO_2 from exhaust gases via reversible adsorptive techniques can promote the development of "waste-to-chemical" technologies, but it relies on the development of efficient sorbent materials that not only show high and reversible adsorption of SO_2, but also are highly robust so that regeneration of the sorbent can be achieved for use over many cycles.

Metal–organic framework (MOF) materials have been studied widely for gas adsorption and separation owing to their high surface area and tuneable pore environment.[8,9] The study of MOF materials as SO_2 reservoirs has seen significant interest recently,[10–12] but only a limited number of MOFs show reversible SO_2 uptake and structural stability upon desorption: for example, Mg-MOF-74 (8.6 mmol g^{-1}),[13] EDTA-MOF-808 (9.8 mmol g^{-1}),[14] [Ni-(bdc)(ted)$_{0.5}$] (10.0 mmol g^{-1}),[15] [Zn_2(L)$_2$(bipy)] (10.9 mmol g^{-1}),[16] SIFSIX-1-Cu (11.0 mmol g^{-1}),[17] ECUT-111 (11.6 mmol g^{-1}),[18] DMOF (13.1 mmol g^{-1}),[19] MFM-300 (Sc)@EtOH (13.2 mmol g^{-1}),[20] MOF-808 (15.3 mmol g^{-1}),[14] MFM-170 (17.5 mmol g^{-1})[21] and MIL-101(Cr)-4F(1 %) (18.4 mmol g^{-1})[22] all at 298 K and 1 bar of SO_2. MOFs constructed from {Zr_6} clusters are renowned for their high stability.[23–25] However, their performance in adsorption of SO_2 has been poorly explored and, to date, only few Zr-MOFs have shown reversible SO_2 adsorption at 298 K and 1 bar, including MFM-601 (12.3 mmol g^{-1})[26] and NU-1000 (10.9 mmol g^{-1}).[27]

Herein, we report a systematic structural and dynamic analysis of adsorption of SO_2 in seven robust Zr-MOFs: UiO-66, UiO-66-NH_2, UiO-66-Cu^{II}, Zr-DMTDC (H_2DMTDC = 3,4-dimethylthieno[2,3-b]thiophene-2,5-dicarboxylic acid), Zr-bptc, MFM-133 and MFM-422. Compared with UiO-66, the introduction of amine groups (UiO-66-NH_2), thienothiophene groups (Zr-DMTDC) or atomically-dispersed Cu^{II} sites (UiO-66-Cu^{II}) afford 76 %, 47 % and 43 % enhancement of SO_2 uptake at 0.1 bar and 298 K, respectively. Zr-bptc exhibits an exceptional SO_2 uptake of

6.2 mmol g^{-1} at 0.1 bar and 298 K and dynamic breakthrough confirms the highly selective capture of SO_2 from a mixture of SO_2/CO_2 (2500 ppm SO_2, 15 % CO_2 diluted in He). In addition, the captured SO_2 in Zr-bptc can be converted to aryl N-amino sulphonamide, an important compound in medicinal chemistry, thus fulfilling the "waste-to-chemicals" target. MFM-422 shows a high Brunauer–Emmett–Teller (BET) surface area of 3296 cm^2 g^{-1} and an exceptional and reversible uptake of SO_2 of 31.3 mmol g^{-1} at 1 bar and 273 K. These materials show high stability with full retention of structure and uptake capacities over multiple cycles of adsorption-desorption of dry SO_2. The adsorption domains and binding dynamics of SO_2 in these MOFs have been studied by in situ synchrotron X-ray powder diffraction (SXPD), inelastic neutron scattering (INS), and synchrotron infrared micro-spectroscopy (microFTIR) to provide key insights into the structures and dynamics of high adsorption of SO_2 in these systems.

Results and Discussion

UiO-66,[28] UiO-66-NH_2,[29] UiO-66-Cu^{II}[30] and Zr-DMTDC[31] are iso-structural and constructed from 12-connected $\{Zr_6(\mu_3\text{-}O)_4(\mu_3\text{-}OH)_4(OOCR)_{12}\}$ clusters bridged by dicarboxylates to give cubic structures of ***fcu*** topology (Figure 1). These structures consist of two types of cages with an octahedral cage (Cage O, diameter of 9–12 Å) connecting to eight tetrahedral cages (Cage T, diameter of 7.3 Å) via triangular faces (Figure 1). The pores of UiO-66-NH_2 and Zr-DMTDC are decorated with free $-NH_2$ and –S– sites, respectively, affording additional binding sites for guest molecules. In UiO-66-Cu^{II}, defect sites with free –OH/$–OH_2$ sites in the pore are decorated with open Cu^{II} sites. Desolvated UiO-66, UiO-66-NH_2, UiO-66-Cu^{II} and Zr-DMTDC show BET surface areas of 1221, 1037, 1068 and 1345 $m^2 g^{-1}$, respectively.

Zr-bptc is built from 12-connected $\{Zr_6(\mu_3\text{-}O)_4(\mu_3\text{-}OH)_4(OOCR)_{12}\}$ clusters and tetracarboxylate ligands in an open framework of ***ftw*** topology.[32] Desolvated Zr-bptc consists of cubic cages (cage A) of diameter 12 Å fused to tetrahedral cages (cage B) of 4.5 Å diameter (Figure 1) with a BET surface area of 960 $m^2 g^{-1}$. MFM-133[33] is constructed from 8-connected $\{Zr_6(OH)_8(OH)_8(OOCR)_8\}$ clusters and $thcb^{4-}$ ligands (H_4thcb = 3,3′,5,5′-tetrakis(4-carboxyphenyl)-2,2′,4,4′,6,6′-hexamethyl-1,1′-biphenyl) to form a ***flu*** topology. MFM-133 shows an axially elongated octahedral cage (10.4 × 10.4 × 25.9 Å) and a BET surface area of 2156 $m^2 g^{-1}$ (Figure 1). A new MOF, MFM-422, is constructed by linking 8-connected $\{Zr_6(OH)_8(OH)_8(OOCR)_8\}$ clusters with the tetratopic ligand 3,3″,5,5″-tetrakis(4-carboxyphenyl)-*p*-terphenyl (H_4tcpt) to give a neutral framework of ***sqc*** topology. MFM-422 is comprised of a trigonal cage (cage B, diameter of 7.7 Å) and a hexagonal cage (cage A, diameter of 30 Å, Figure 1). Desolvated MFM-422 shows a BET surface area of 3296 $m^2 g^{-1}$ and a high thermal stability up to 500 °C (Figures S43–S44).

Gravimetric adsorption isotherms of SO_2 have been recorded for these MOFs at 273–298 K and from 0–1 bar (Figures 2a,b, S1–S7 and Table 1). MFM-422 shows a SO_2 uptake of 31.3 mmol g^{-1} at 273 K and 1.0 bar, comparable to the record previously achieved by UR3-MIL-101(Cr) (36.7 mmol g^{-1}) under the same conditions.[34] At 298 K and 1 bar, all 7 MOFs, i.e., UiO-66, UiO-66-NH_2, UiO-66-Cu^{II}, Zr-DMTDC, Zr-bptc, MFM-133 and MFM-422, show fully reversible uptakes of SO_2 of 8.6, 8.8, 8.2, 9.6, 7.8, 8.9 and 13.6 mmol g^{-1}, respectively (Figures 2b and S1–S7). The multiple cycles of adsorption-desorption of SO_2 for all samples at 298 K show little change in the capacity, demonstrating excellent stability towards dry SO_2 (Figures S1–S7, S30–S35). The comparable adsorption uptakes of UiO-66, UiO-66-NH_2 and UiO-66-Cu^{II} at 1 bar (8.2–8.8 mmol g^{-1}) suggest that decoration of the pore environment with functional groups or open Cu^{II} sites has little impact on the total uptake capacity, which is determined primarily by the surface area. The slightly higher uptake of Zr-DMTDC (9.6 mmol g^{-1}) is consistent with its higher surface area (1345 $m^2 g^{-1}$), compared with the other three UiO-66 materials. In contrast, enhancements in the uptake at 0.1 bar were observed for UiO-66-NH_2, UiO-66-Cu^{II} and

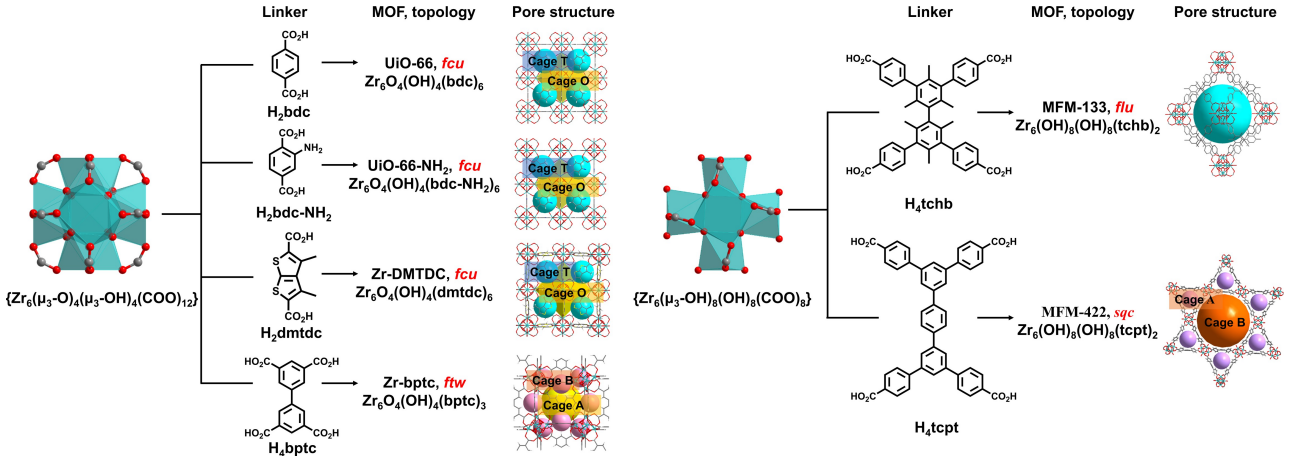

Figure 1. Views of $\{Zr_6\}$-clusters, linkers and structures of the Zr-based MOFs used in this study (Zr, aqua; C, grey; O, red; H, white; S, yellow).

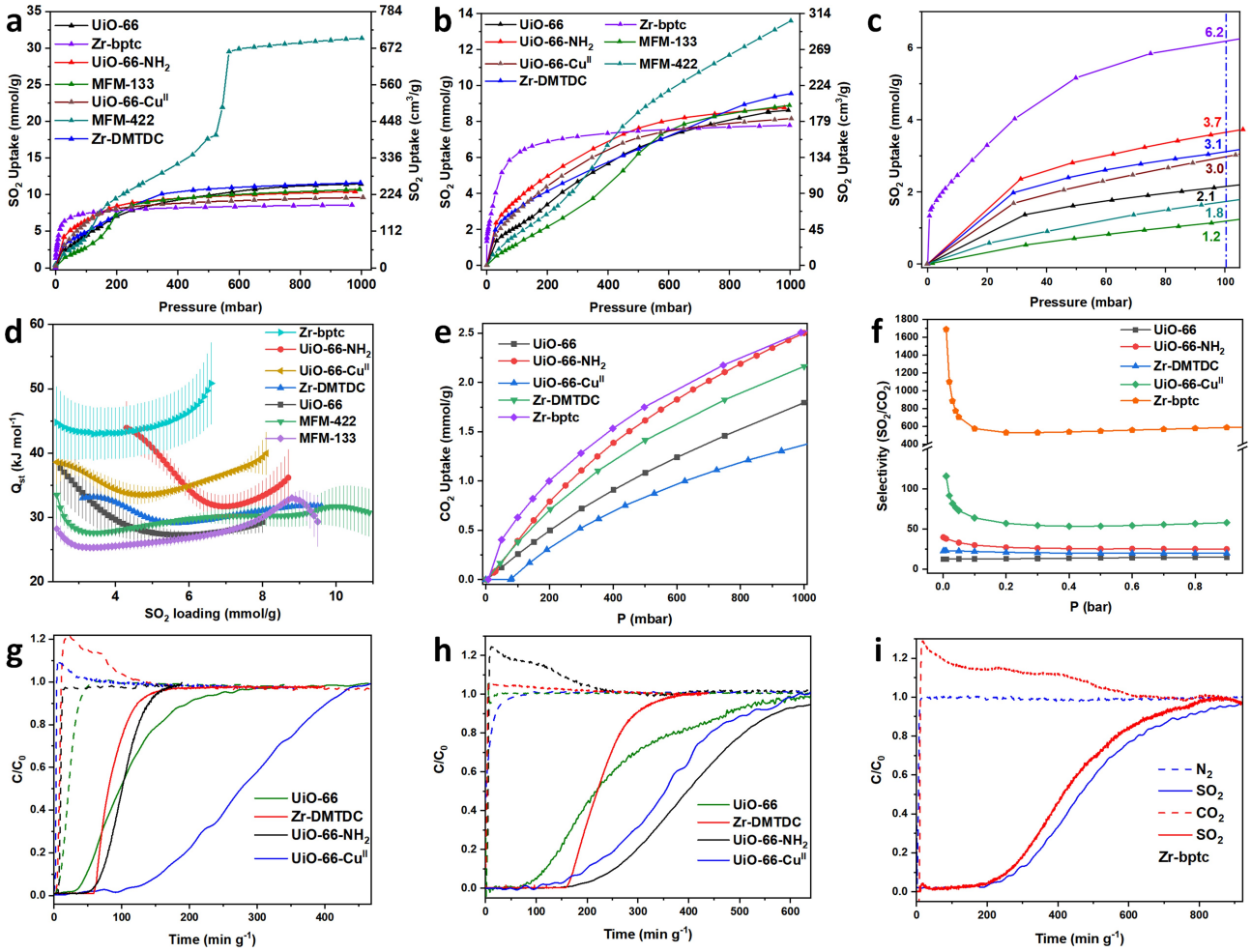

Figure 2. Gas adsorption, thermodynamic, selectivity and separation data. SO_2 adsorption isotherms at (**a**) 273 K and 1 bar and (**b**) 298 K and 1 bar (desorption data are omitted for clarity and shown in Figures S1–S7); (**c**) SO_2 adsorption isotherms from 0 to 0.1 bar at 298 K; (**d**) variation of Q_{st}; (**e**) CO_2 adsorption isotherms for Zr-bptc, Zr-DMTDC and UiO-66 materials at 298 K and 1 bar; (**f**) comparison of IAST selectivities of SO_2/CO_2 (1 : 99) for Zr-bptc, Zr-DMTDC and UiO-66 materials at 298 K; (**g**) breakthrough plots for a SO_2/CO_2 mixture (2500 ppm SO_2, 15 % CO_2 in He, total flow rate: 20 mL min^{-1}) in Zr-DMTDC and UiO-66 materials at 298 K (solid line: SO_2; dashed line: CO_2); (**h**) breakthrough plots for a SO_2/N_2 mixture (2500 ppm SO_2, 75 % N_2 in He, total flow rate: 14 mL min^{-1}) in Zr-DMTDC and UiO-66 materials at 298 K (solid line: SO_2; dashed line: N_2); (**i**) breakthrough plots for a SO_2/N_2 mixture (2500 ppm SO_2, 75 % N_2 in He, total flow rate: 40 mL min^{-1}) and (2500 ppm SO_2, 15 % CO_2 in He, total flow rate: 40 mL min^{-1}) in Zr-bptc at 298 K (blue: SO_2/N_2 mixture; red: SO_2/CO_2 mixture).

Table 1: Summary of BET surface areas, SO_2 uptakes and Q_{st} and IAST selectivities in Zr-MOFs.

MOFs	BET [m^2 g^{-1}]	SO_2 Uptake [mmol g^{-1}] at 1 bar 298 K	273 K	SO_2 Q_{st} [kJ mol^{-1}]	Selectivity SO_2/CO_2 (1/99)	SO_2/N_2 (1/99)
Zr-bptc	960	7.8	8.6	45–50	600	> 5 000
UiO-66-Cu^{II}	1068	8.2	9.6	38–34	54	3 100
UiO-66-NH_2	1037	8.8	10.5	44–32	25	486
Zr-DMTDC	1345	9.6	11.6	32–29	20	280
UiO-66	1221	8.6	11.5	37–27	13	208
MFM-133	2156	8.9	10.7	31–27	–	–
MFM-422	3296	13.6	31.3	26–19	–	–

Zr-DMTDC, compared with UiO-66 (uptakes of 3.7, 3.0, 3.1 and 2.1 mmol g^{-1}, respectively, Figure 2c). This demonstrates that the introduction of accessible –NH_2, Cu^{II} or R-S-R sites into the pores can increase the binding strength with SO_2 molecules. Interestingly, Zr-bptc displays an extremely high uptake of 6.2 mmol g^{-1} at 0.1 bar and 298 K, suggesting potential for selective adsorption of SO_2 at low concentration. The isosteric heats of adsorption (Q_{st}) for SO_2 uptake show decreasing values of 45–50, 44–32, 38–34, 32–29, 37–27, 31–27 and 26–19 kJ mol^{-1} for Zr-bptc, UiO-66-

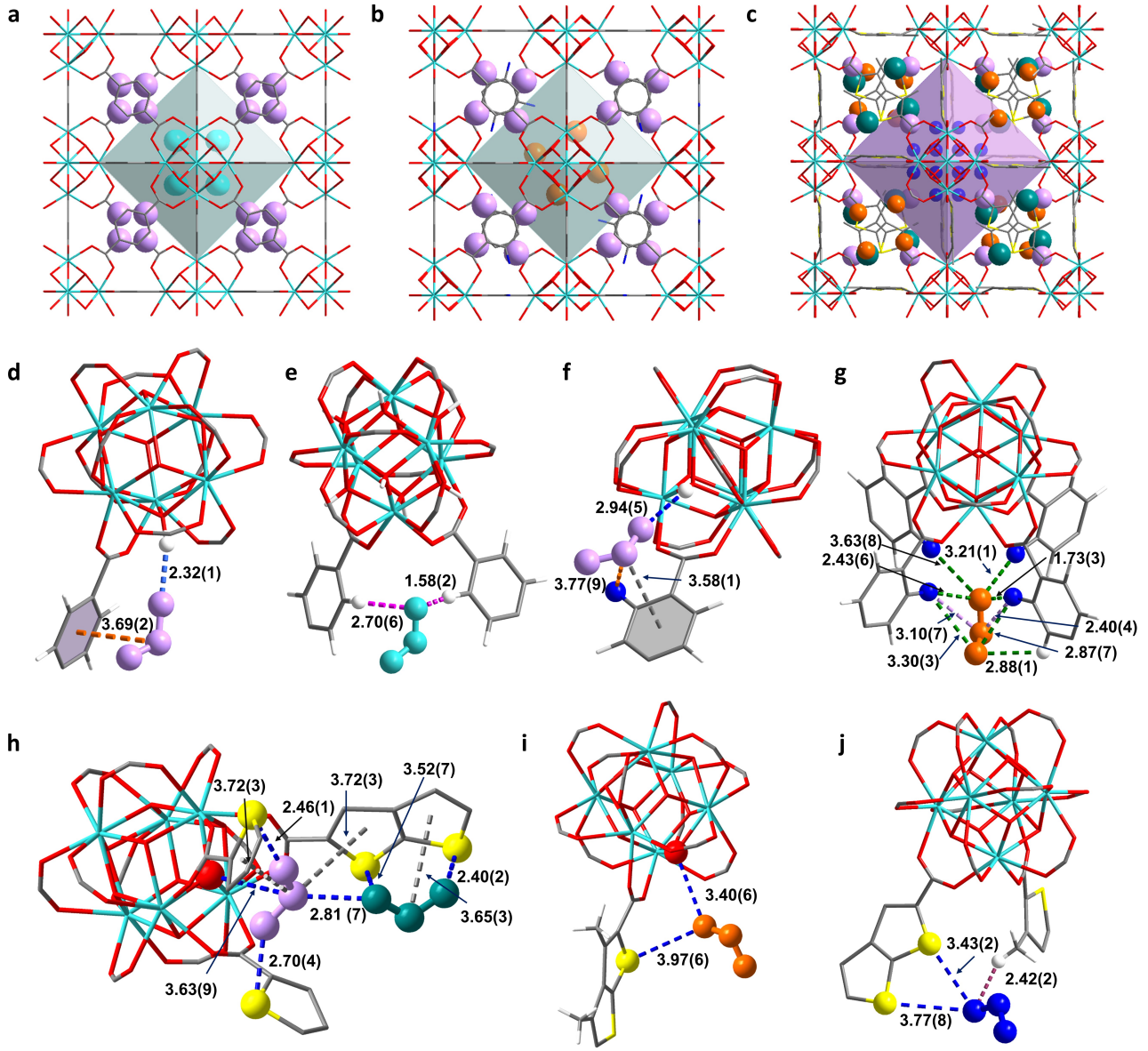

Figure 3. Views of binding of SO_2 in (**a**) UiO-66 (site I in cage T: lavender; site II in cage O: cyan); (**b**) UiO-66-NH_2 (site I' in cage T: lavender; site II' in cage O: orange); (**c**) Zr-DMTDC (site I'', II'' and III'' in cage T: teal, lavender and orange, respectively; site IV' in cage O: blue); (**d**) UiO-66 at site I (SO_2: lavender); (**e**) UiO-66 at site II (SO_2: cyan); (**f**) UiO-66-NH_2 at site I' (SO_2: lavender); (**g**) UiO-66-NH_2 at site II' (SO_2: orange); (**h**) Zr-DMTDC at site I'' (SO_2: teal) and II'' (SO_2: lavender); (**i**) Zr-DMTDC at site III'' (SO_2: orange); (**j**) Zr-DMTDC at site IV'' (SO_2: blue) (in framework Zr: cyan; O: red; S: yellow; C: dark grey and H: white). All units are quoted in Å.

NH_2, UiO-66-Cu^{II}, Zr-DMTDC, UiO-66, MFM-422 and MFM-133, respectively. Compared with UiO-66, the materials UiO-66-NH_2, UiO-66-Cu^{II} and Zr-DMTDC show higher values for Q_{st}, consistent with the enhanced adsorption at low pressure. The relatively low values of Q_{st} for MFM-133 and MFM-422 are consistent with their large pores, reducing the strength of host–guest interactions.

Adsorption isotherms of CO_2 and N_2 have also been recorded for Zr-bptc, UiO-66-NH_2, UiO-66-Cu^{II}, Zr-DMTDC and UiO-66 to assess the adsorption selectivity (Figures 2e, S8–S12, Table S1). At 298 K, Zr-bptc displays CO_2 uptakes of 2.5 and 0.82 mmol g^{-1} at 1.0 and 0.15 bar, respectively. While UiO-66-NH_2 and Zr- DMTDC display 58 % and 42 % enhancements in the CO_2 uptake at 0.15 bar and 298 K compared with UiO-66, UiO-66-Cu^{II} shows a reduction of CO_2 uptake of 47 % at 0.15 bar and 298 K (Figures 2e). Thus, the latter has great potential for selective adsorption of SO_2. Analysis of pure-component isotherms via ideal adsorbed solution theory (IAST)[35] affords adsorption selectivities for mixtures of SO_2/CO_2 (1/99) and SO_2/N_2 (1/99) (Figure 2f and S13) for Zr-bptc, UiO-66-NH_2, UiO-66-Cu^{II}, Zr-DMTDC and UiO-66. Zr-bptc displays high selectivities of 600 for SO_2/CO_2 and >5000 for SO_2/N_2; the very high IAST selectivity is subject to uncertainties owing to the extremely low adsorption of N_2. UiO-66-Cu^{II}, UiO-66-NH_2, Zr-DMTDC and UiO-66 display IAST selectivities for

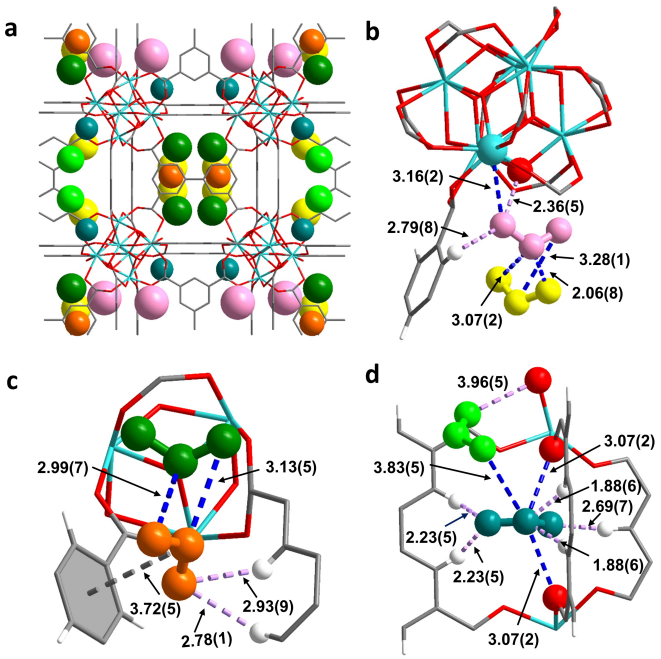

Figure 4. Views of the binding sites of SO_2 in (**a**) Zr-bptc (site I, II, III, IV and V in cage A: rose, yellow, dark green, green and orange, respectively; site VI in cage B: teal); (**b**) Zr-bptc at sites I (SO_2: rose) and II (SO_2: yellow); (**c**) Zr-bptc at site III (SO_2: dark green) and V (SO_2: orange); (**d**) Zr-bptc at site IV (SO_2: green) and VI (SO_2: teal) (in framework Zr: cyan; O: red; S: yellow; C: dark grey and H: white). All units are quoted in Å.

SO_2/CO_2 of 54, 25, 20 and 13, and for SO_2/N_2 of 3100, 486, 280 and 208, respectively. To confirm the selective capture of SO_2 under realistic concentrations,[36] fixed-beds packed with these MOFs were studied by dynamic breakthrough experiments with a mixture of SO_2/CO_2 (2500 ppm SO_2/15 % CO_2 in He) at 298 K and 1.0 bar. UiO-66, UiO-66-NH_2, Zr-DMTDC and UiO-66-Cu^{II} exhibit retention times for SO_2 in the expected order of 33, 53, 58 and 100 min g^{-1}, respectively (Figure 2g). The same sequence was observed in the separation of the mixture of SO_2/N_2 (2500 ppm/75 %) with retention times of 80, 175, 157 and 175 min g^{-1} for UiO-66, UiO-66-NH_2, Zr-DMTDC and UiO-66-Cu^{II}, respectively (Figure 2h). Zr-bptc shows highly selective retention of SO_2 at 213 and 235 min g^{-1} for mixtures of SO_2/CO_2 (2500 ppm SO_2/15 % CO_2 in He) and SO_2/N_2 (2500 ppm SO_2/75 % CO_2 in He), respectively (Figure 2i). Thus, the breakthrough results are fully consistent with the isotherm data and confirm the positive role of open Cu^{II} sites on selective SO_2 adsorption.

Rietveld refinements of the high-resolution SXPD data of SO_2-loaded UiO-66 [$Zr_6O_4(OH)_4(bdc)_6\cdot(SO_2)_{7.7}$] reveal two binding sites I and II located in cage T ($SO_2/\{Zr_6\}=5.1$) and cage O ($SO_2/\{Zr_6\}=2.6$), respectively (Figure 3a). The hydrogen bond [OSO···μ_3-HO = 2.32(1) Å] and dipole–dipole interaction [O_2S···phenyl ring = 3.69(2) Å] stabilise SO_2 (I) (Figure 3d). SO_2 (II) is stabilised by two hydrogen bonds [OSO···H–C = 1.58(2), 2.70(6) Å] (Figure 3e). In SO_2-loaded UiO-66-NH_2 [$Zr_6O_4(OH)_4(bdc\text{–}NH_2)_6\cdot(SO_2)_{8.1}$], two binding sites I′ and II′ are observed in cage T ($SO_2/\{Zr_6\}=4.7$) and cage O ($SO_2/\{Zr_6\}=3.4$), respectively (Figure 3b). Due to the presence of active –NH_2 groups, the adsorbed SO_2 molecules are stabilised strongly by the formation of supramolecular interactions between –NH_2 groups and SO_2 molecules. A dipole–dipole interaction [NH_2···SO_2 = 3.77 (9) Å] was identified and works together with an interaction [O_2S···phenyl ring = 3.58(1) Å] and hydrogen bonding [OSO···μ_3-HO = 2.94(5) Å] that stabilise SO_2 binding at site I′ (Figure 3f). In addition, seven hydrogen bonds were identified [OSO···H–C = 2.88(1) Å, SO_2···NH_2 = 1.73(3), 2.43(6), 2.87(7), 3.21(1), 3.30(3) and 3.63(8) Å], which work together with two further dipole–dipole interactions [O_2S···NH_2 = 2.40(4) and 3.10(7) Å] to stabilise SO_2 at site II′ (Figure 3g). The additional hydrogen bonds and dipole–dipole interactions demonstrate enhanced binding of SO_2 in UiO-66-NH_2, consistent with the increased SO_2 adsorption at low pressure.

In SO_2-loaded Zr-DMTDC [$Zr_6O_4(OH)_4(DMTDC)_2\cdot(SO_2)_{13.1}$], four binding sites were revealed (I″-IV″). Sites I″, II″ and III″ are localised in cage T ($SO_2/\{Zr_6\}=4.2$, 4.1 and 2.5, respectively) (Figure 3c). The SO_2 molecule at site I″ is stabilised by the formation of three dipole–dipole interactions [OSO···S-ring = 2.40(2) and 3.52 (7) Å; O_2S···thiophene ring = 3.65(3) Å] (Figure 3h). The SO_2 molecules at site II″ are stabilised further by four dipole–dipole interactions [OSO···S-ring = 2.46(1) and 2.70(4) Å; O_2S···thiophene ring = 3.72(3) and 3.72(3) Å] and supramolecular interaction [O_2S···μ_3-O = 3.63(9) Å]. In addition, dipole–dipole interaction between SO_2 at sites I″ and II″ [OSO(I″)···SO_2(II″) = 2.81(7) Å] was identified (Figure 3h), which is not observed in either UiO-66 or UiO-66-NH_2 and may result from the slightly enlarged pore size. The formation of dipole–dipole interactions [O_2S···μ_3-O = 3.40(6) Å] and [OSO···S-ring = 3.97(6) Å] were identified between SO_2(III″) and the framework (Figure 3i). Site IV″ is in the cage O and stabilised by two dipole–dipole interactions [OSO···S-ring = 3.43(2) and 3.77(8) Å] and a hydrogen bond [OSO···H_3C = 2.42(2) Å] (Figure 3j). This crystallographic study enables direct observation of host–guest interactions, and revealed that the introduction of heteroatom S dominated the supramolecular interactions facilitating the immobilisation of SO_2 at low pressure.

In SO_2-loaded Zr-bptc, [$Zr_6O_4(OH)_4(bptc)_3\cdot(SO_2)_{5.8}$], six binding sites were revealed (I–VI) (Figure 4a). Sites I, II, III, IV and V are localised in cage A with $SO_2/\{Zr_6\}$ ratios of 1.7, 1.1, 1.0, 0.61 and 0.96, respectively, and Site VI located at cage B with a $SO_2/\{Zr_6\}$ ratio of 0.43. SO_2 molecules at site I were stabilised by Zr^{IV} sites [OSO···Zr = 3.16(2) Å] and by two hydrogen bonds [OSO···H–C = 2.79(8) Å and OSO···μ_3-OH = 2.36(5) Å] (Figure 4b). SO_2 molecules at site II are immobilised by three dipole–dipole interactions [OSO(II)···SO_2(I) = 2.06(8) and 3.07(2) Å, OSO(I)···SO_2(II) = 3.28(1) Å] with SO_2 at site I (Figure 4b). SO_2 molecules at site III are stabilised by dipole–dipole interactions [O_2S-(III)···OSO(V) = 2.99(7) Å, OSO(III)···SO_2(V) = 3.13(5) Å] with SO_2 at site V immobilised by dipole–dipole interactions [O_2S···phenyl ring = 3.72(5) Å] and two-fold electrostatic interactions [OSO···H–C = 2.78(1) and 2.93(9) Å] (Fig-

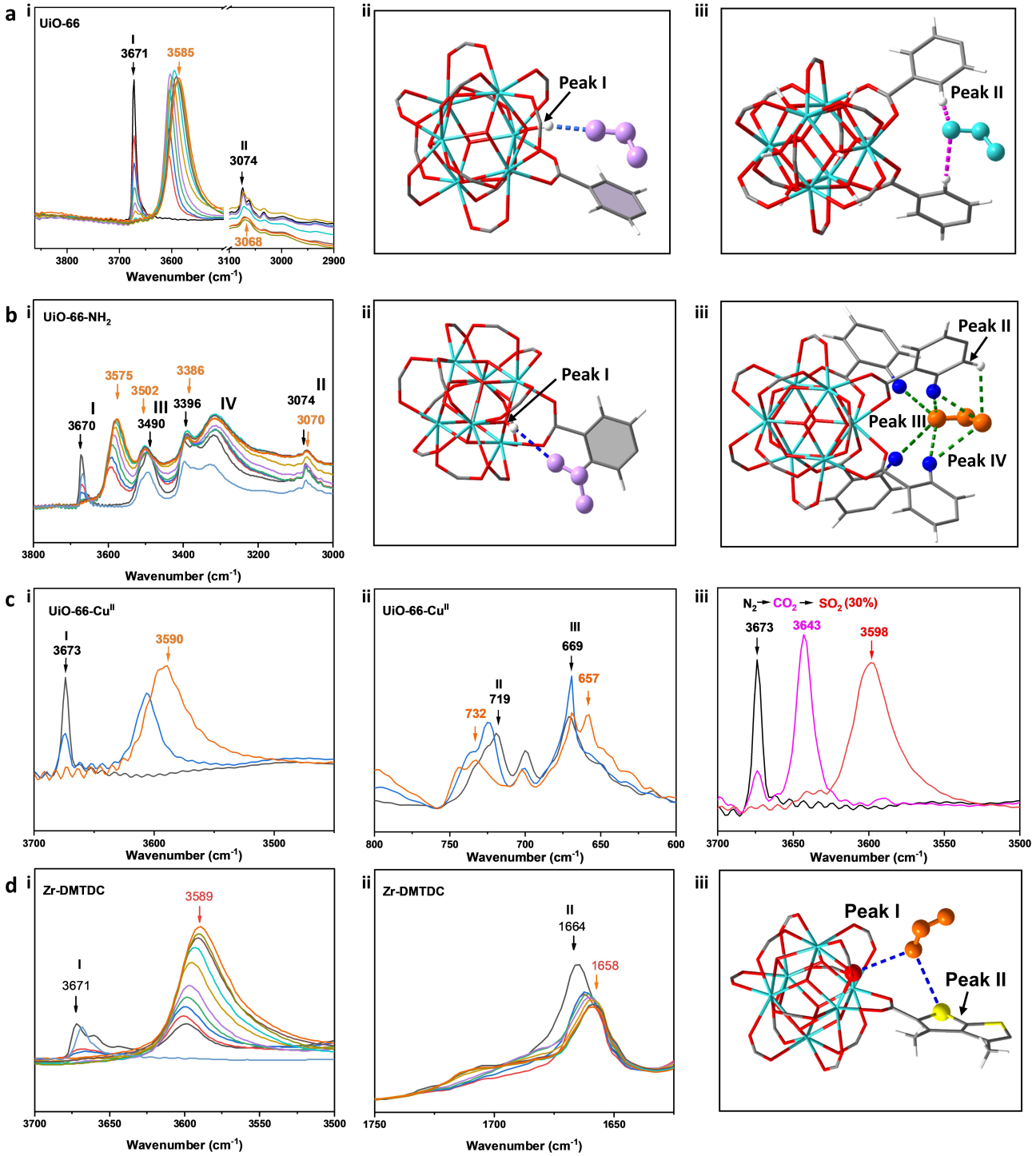

Figure 5. (**a**) (i). IR spectra showing the $\nu(\mu_3\text{-OH})$ and ν(-CH) stretching region for UiO-66 at various loadings of SO_2; (ii–iii) views of corresponding structures. (**b**) (i) IR spectra showing the $\nu(\mu_3\text{-OH})$, $\nu(\text{-NH}_2)$ and ν(-CH) stretching region for UiO-66-NH_2 at various loadings of SO_2; (ii-iii) views of corresponding structures; (**c**) IR spectra of (i) $\nu(\mu_3\text{-OH})$, (ii) ν(Cu–OH) and $\nu(\text{Cu–OH}_2)$ stretching region for UiO-66-Cu^{II} at 2% (blue) and 100% (orange) loading of SO_2 (other loadings are omitted for clarity and shown in the Supplementary Information Figures S21–S22); iii) IR spectra of the $\nu(\mu_3\text{-OH})$ stretch region for bare (black), 100% CO_2-loading (purple) and 30% SO_2-loading for CO_2 displacement (red) in UiO-66-Cu^{II}; (**d**) IR spectra of (i) $\nu(\mu_3\text{-OH})$ and (ii) ν(S–C) stretching region for Zr-DMTDC at various loadings of SO_2; (iii). Views of corresponding structures (in various SO_2-loading experiments: black: bare MOF, red: 1% SO_2-loading, blue: 2% SO_2-loading, green: 5% SO_2-loading, violet: 10% SO_2-loading, dark yellow: 20% SO_2-loading, cyan: 40% SO_2-loading, light wine: 60% SO_2-loading, wine: 80% SO_2-loading, orange: 100% SO_2-loading).

ure 4c). SO_2 molecules at site IV are stabilised by a weak hydrogen bond [OS<u>O</u>···μ_3-H<u>O</u> = 3.96(5) Å] and dipole–dipole interaction [OS<u>O</u>(IV)···<u>S</u>O_2(VI) = 3.83(5) Å] with SO_2 at site VI (Figure 4d). SO_2 molecules at site VI sit at the centre of

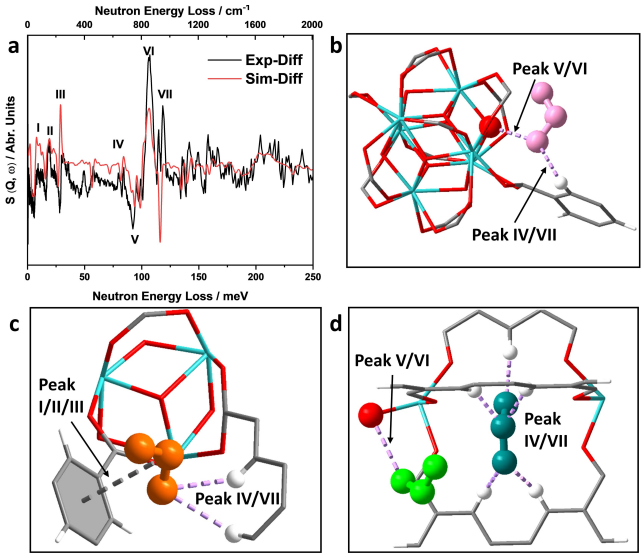

Figure 6. (**a**) Comparison of the difference plots for experimental and DFT-calculated INS spectra of bare and SO_2-loaded Zr-bptc. No scale factor was used for the DFT calculations. *S*, dynamic structure factor; *Q*, difference between incoming and outgoing wave vector; ω, the energy change experienced by the sample; (**b–d**) Views of corresponding structures.

cage B and are immobilised by five hydrogen bonds [OSO···H–C = 1.88(6), 1.88(6), 2.23(5), 2.23(5) and 2.69 (7) Å] and two dipole–dipole interactions [O_2S···OOC = 3.07(2) and 3.07(2) Å] (Figure 4d). In contrast to the host–guest binding observed in SO_2-loaded UiO-66 type systems, Zr^{IV} sites, the strong hydrogen bonding at site I, unique dipole–dipole interactions between SO_2(VI) and carboxylic groups and multiple strong hydrogen bonding at site VI jointly facilitate the exceptional SO_2 uptake at low pressure.

The binding dynamics of adsorption of SO_2 (0–1 bar) in the UiO-66 type systems have been analysed by in situ synchrotron infrared micro-spectroscopy. For all the MOFs, clear binding of SO_2 to the hydroxyl group is observed with a red shift of the –OH stretching vibration at ≈3671 cm^{-1} by 86, 95, 83 and 82 cm^{-1} in UiO-66, UiO-66-NH_2, UiO-66-Cu^{II} and Zr-DMTDC, respectively (Figures 5ai–di). There is clear evidence for enhanced interaction of SO_2 via hydrogen bonding to –NH_2 groups ([NH_2···OSO], the characteristic NH_2 band shifting from 3490 to 3502 cm^{-1} and 3396 to 3386 cm^{-1} (Figure 5b). Dipole interactions are observed to the Cu^{II} sites ([OSO····Cu–OH], with the characteristic Cu-OH band shifting from 719 to 732 cm^{-1}. Formation of [OSO···Cu–OH_2] interactions leads to a new band at 657 cm^{-1} assigned to the CuO stretching vibration[37] (Figure 5cii), while the thiophene system leads to [OSO···S] interactions with a characteristic shift in the S–C stretch from 1664 to 1658 cm^{-1}[38] (Figure 5dii). The displacement and cooperative binding of SO_2 and CO_2 was investigated in UiO-66-Cu^{II}. The $\nu(\mu_3$-OH) mode was monitored to examine the displacement of bound CO_2 by SO_2 (Figures 5ciii, S26). Upon loading of CO_2 to 1 bar, the peak areas for the $\nu(\mu_3$-OH) stretch corresponding to the bare and CO_2-loaded materials are approximately equal. Due to weak interaction between CO_2 and the μ_3-OH group, the bare μ_3-OH band is not fully depleted but a new peak at 3643 cm^{-1} appears and is assigned to the [OH···OCO] band (Figure 5ciii).

Upon stepwise dosing of the CO_2-saturated material with SO_2 (i.e., tuning the SO_2/CO_2 mixture from 0/100 to 100/0 while maintaining a total pressure of 1.0 bar), there is a steady change in the $\nu(\mu_3$-OH) region that includes new bands appearing in a similar manner to the pure SO_2 experiment, indicating that bound CO_2 does not impede SO_2 adsorption (Figure S26). Upon 30 % SO_2-loading, the characteristic [OH···OCO] band has fully disappeared showing that SO_2 readily displaces bound CO_2 in the pore as a result of stronger binding. Hence, selective capture of SO_2 from a mixture of SO_2/CO_2 can be achieved as demonstrated in separation experiments. Furthermore, 40 %, 45 % and 50 % SO_2-loadings fully displace CO_2 in UiO-66-NH_2, Zr-DMTDC and UiO-66, respectively (Figures S24–27). The competitive binding studies of SO_2/CO_2 further confirm enhanced SO_2 binding in the decorated MOFs. The decreasing partial pressure of SO_2 on full displacement of CO_2 in UiO-66-Cu^{II}, UiO-66-NH_2 and Zr-DMTDC is consistent with that observed in static and dynamic adsorption studies.

In situ INS, coupled with DFT calculations, enables the visualization of binding dynamics for SO_2-loaded Zr-bptc. Seven major changes in the INS spectra were observed on the adsorption of SO_2 in Zr-bptc (Figure 6a). Peaks I-III occur at low energy transfer (< 60 meV) and Peaks IV-VII at the high energy region (80–120 meV). Peak I (8.3 meV) is assigned to the flapping mode of the aromatic ring and peaks II (19.3 meV) and III (29.6 meV) are due to aromatic deformation. Peaks IV (83.7 meV) and VII (118 meV) are assigned to C–H out-of-plane bending modes with H moving in the same direction and opposite directions, respectively. The changes in peaks I, II, III, IV and VII suggest interactions between adsorbed SO_2 molecules and the aromatic moieties, consistent with the crystallographic analyses (Figures 6b–d). Peaks V (92.9 meV) and VI (106.5 meV) are assigned to μ_3-OH wagging and twisting, respectively, and their changes support the formation of hydrogen bonds [OSO···μ_3-HO] that were observed in the crystallographic analysis (Figure 6b and 6d).

Unlike FGD technology, where SO_2 is bound permanently to sorbent materials to form solid inorganic wastes, the SO_2 captured by these Zr-MOFs remains available to undergo chemical transformation to valuable products. Here, a proof-of-concept experiment on aminosulfonylation[39,40] using the SO_2-loaded Zr-bptc was conducted, and quantitative conversion of the captured SO_2 was achieved to give 4-methoxyl-aryldiazonium tetrafluoroborate in 85 % yield (Scheme 1). Upon regeneration, Zr-bptc can be used for at least 3 cycles without any change in the crystal structure or porosity of the material (Figure S46 and Table S5), thus demonstrating its great potential of the capture and conversion of waste SO_2 to fine chemicals.

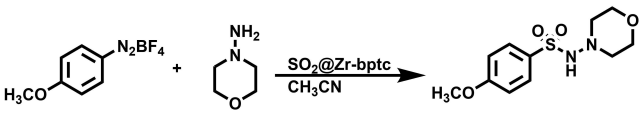

Scheme 1. Conversion of captured SO_2 in Zr-bptc for the synthesis of fine chemicals; 1 equivalent of 4-methoxy-aryldiazonium tetrafluoroborate and 5 equivalents of amine and SO_2-loaded Zr-bptc were reacted at room temperature for 1 h.

Conclusion

Powerful drivers exist for the development of new regenerable sorbents for SO_2 to enable its recovery from exhaust gases and conversion into chemical feedstocks. The highly corrosive and reactive nature of SO_2 leads generally to severe structural degradation of sorbent materials. We report the positive impacts on low pressure SO_2 uptake by introducing functional groups and atomically-dispersed Cu^{II} sites into a family of Zr-MOFs. Owing to the confined metal–ligand cages in Zr-bptc, an exceptional uptake of SO_2 (6.2 mmol g^{-1}) was observed at 0.1 bar and 298 K. Furthermore, the captured SO_2 in Zr-bptc can be converted readily into fine chemicals, paving new pathways to "waste-to-chemicals" technologies. In situ SXPD, microFTIR and INS studies, coupled with DFT calculations, unravel the molecular details of host–guest binding that result in the enhancement of SO_2 adsorption at low pressure in these materials. These studies confirm that control of pore environments is an important approach for improving the adsorption of SO_2.

Associated Content

Additional crystallographic information, gas adsorption data, thermogravimetric analysis, density function theory (DFT) calculations and breakthrough data are available in the Supporting Information. The crystal structures of $[Zr_6(OH)_8(OH)_8(tcpt)_2]$, $[Zr_6O_4(OH)_4(bptc)_3\cdot(SO_2)_{5.8}]$, $[Zr_6O_4(OH)_4(DMTDC)_6\cdot(SO_2)_{13.1}]$, $[Zr_6O_4(OH)_4(bdc)_6\cdot(SO_2)_{7.7}]$ and $[Zr_6O_4(OH)_4(bdc\text{–}NH_2)_6\cdot(SO_2)_{8.1}]$ are available free of charge from the Cambridge Crystallographic Data Centre (Deposition Numbers 2132832, 2151090, 2151089, 2151088 and 2151087).

Acknowledgements

We thank EPSRC (EP/I011870), the Royal Society and The University of Manchester for funding. This project has received funding from the European Research Council (ERC) under the European Union's Horizon 2020 research and innovation programme (grant agreement No 742401, *NANOCHEM*). We are grateful to Diamond Light Source and Oak Ridge National Laboratory (ORNL) for access to Beamlines I11/B22 and VISION, respectively. A portion of this research used resources at the Spallation Neutron Source, a DOE Office of Science User Facility operated by the Oak Ridge National Laboratory. The computing resources were made available through the VirtuES and the ICE-MAN projects, funded by Laboratory Directed Research and Development program and Compute and Data Environment for Science (CADES) at ORNL.

Conflict of Interest

The authors declare no conflict of interest.

Data Availability Statement

The data that support the findings of this study are available in the supplementary material of this article.

Keywords: Capture · Conversion · Crystallography · Metal–Organic Frameworks · Sulfur Dioxide

[1] H. Muller, *Sulfur Dioxide, Vol. 35*, Wiley-VCH, Weinheim, **2012**.
[2] U.S. Energy Information Administration. International Energy Outlook 2019; U.S. Energy Information Administration: Washington, DC, 2019.
[3] European Environment Agency (EEA). Sulphur dioxide (SO_2) emissions. Indicator codes: APE 001, https://www.eea.europa.eu/data-and-maps/indicators/eea-32-sulphur-dioxide-so2-emissions-1, **2015**. (Accessed October 2019).
[4] T. Vandyck, K. Keramidas, A. Kitous, J. Spadaro, R. Dingene, M. Holland, B. Saveyn, *Nat. Commun.* **2018**, *9*, 4939.
[5] L. Zhang, W. Liu, K. Hou, J. Lin, C. Song, C. Zhou, B. Huang, X. Tong, J. Wang, W. Rhine, Y. Jiao, Z. Wang, R. Ni, M. Liu, L. Zhang, Z. Wang, Y. Wang, X. Li, S. Liu, Y. Wang, *Nat. Commun.* **2019**, *10*, 3741.
[6] Editorial, *Nat. Commun.* **2021**, *12*, 5824.
[7] G. Cheng, C. Zhang, *Pol. J. Environ. Stud.* **2018**, *27*, 481–489.
[8] H. Li, L. Li, R. Lin, W. Zhou, Z. Zhang, S. Xiang, B. Chen, *EnergyChem* **2019**, *1*, 100006.
[9] X. Zhao, Y. Wang, D. Li, X. Bu, P. Feng, *Adv. Mater.* **2018**, *30*, 1705189.
[10] X. Han, S. Yang, M. Schröder, *Nat. Chem. Rev.* **2019**, *3*, 108–118.
[11] E. Martínez-Ahumada, A. López-Olvera, V. Jancik, J. Sánchez-Bautista, E. González-zamora, V. Martis, D. Williams, I. Ibarra, *Organometallics* **2020**, *39*, 883–915.
[12] E. Martínez-Ahumada, M. Díaz-Ramírez, M. Velásquez-Hernández, V. Jancik, I. Ibarra, *Chem. Sci.* **2021**, *12*, 6772–6799.
[13] T. Grant Glover, G. Peterson, B. Schindler, D. Britt, O. Yaghi, *Chem. Eng. Sci.* **2011**, *66*, 163–170.
[14] Z. Zhang, B. Yang, Y. Wu, W. Zhang, Y. Ma, *Sep. Purif. Technol.* **2021**, *276*, 119349.
[15] K. Tan, P. Canepa, Q. Gong, J. Liu, D. Johnson, A. Dyevoich, P. Thallapally, T. Thonhauser, J. Li, Y. Chabal, *Chem. Mater.* **2013**, *25*, 4653–4662.
[16] S. Glomb, D. Woschko, G. Makhloufi, C. Janiak, *ACS Appl. Mater. Interfaces* **2017**, *9*, 37419–37434.
[17] X. Cui, X. W. Wang, L. Yang, R. Krishma, Z. Zhang, Z. Bao, H. Wu, Q. Ren, W. Zhou, B. Chen, H. Xing, *Adv. Mater.* **2017**, *29*, 1606929.
[18] Y. Fan, H. Zhang, M. Yin, R. Krishna, X. Feng, L. Wang, M. Luo, F. Luo, *Inorg. Chem.* **2021**, *60*, 4–8.

[19] S. Xing, J. Liang, P. Brandt, F. Schafer, A. Nugnen, T. Heinen, I. Boldog, M. Lange, O. Weingart, C. Janiak, *Angew. Chem. Int. Ed.* **2021**, *60*, 17998–18005; *Angew. Chem.* **2021**, *133*, 18145–18153.
[20] J. Zárate, E. Sanchez-Gonzalez, D. Williams, E. Gonzalez-Zamora, V. Martis, A. Martinez, J. Balmaseda, G. Maurin, I. Ibarra, *J. Mater. Chem. A* **2019**, *7*, 15580–15584.
[21] G. Smith, J. Eyley, X. Han, X. Zhang, J. Li, N. Jacques, H. Godfrey, S. Argent, L. McPherson, S. Teat Y Cheng, M. Frogley, G. Cinque, S. Day, C. Tang, T. Easun, S. Rudic, A. Ramirez-Cuesta, S. Yang, M. Schröder, *Nat. Mater.* **2019**, *18*, 1358–1365.
[22] E. Martínez-Ahumada, M. Diaz-Ramirez, H. Lara-Garcia, D. Williams, V. Martis, V. Jancik E Lima, I. Ibarra, *J. Mater. Chem. A* **2020**, *8*, 11515–11520.
[23] S. Yuan, L. Feng, K. Wang, J. Pang, M. Bosch, C. Lollar, Y. Sun, J. Qin, X. Yang, P. Zhang, Q. Wang, L. Zou, Y. Zhang, L. Zhang, Y. Fang, J. Li, H. Zhou, *Adv. Mater.* **2018**, *30*, 1704303.
[24] D. Zou, D. Liu, *Mater. Today Chem.* **2019**, *12*, 139–165.
[25] Y. Bai, Y. Dou, L. Xie, W. Rutledge, J. Li, H. Zhou, *Chem. Soc. Rev.* **2016**, *45*, 2327–2367.
[26] J. Carter, X. Han, F. Moreau, I. Silva, A. Nevin, H. Godfrey, C. Tang, S. Yang, M. Schröder, *J. Am. Chem. Soc.* **2018**, *140*, 15564–15567.
[27] S. Gorla, M. Diaz-Ramirez, N. Abeynayake, D. Kaphan, D. Williams, V. Martis, H. Lara-Garcia, B. Donnadieu, N. Lopez, I. Ibarra, V. Montiel-Palma, *ACS Appl. Mater. Interfaces* **2020**, *12*, 41758–41764.
[28] J. Cavka, S. Jakobsen, U. Olsbye, N. Guillou, C. Lamberti, S. Bordiga, K. Lillerud, *J. Am. Chem. Soc.* **2008**, *130*, 13850–13851.
[29] S. Garibay, S. Cohen, *Chem. Commun.* **2010**, *46*, 7700–7702.
[30] Y. Ma, X. Han, S. Xu, Z. Wang, W. Li, I. Silva, S. Chansai, D. Lee, Y. Zou, M. Nikiel, P. Manuel, A. Sheveleva, F. Tuna, E. McInnes, Y. Cheng, S. Rudic, A. Ramirez-Cuesta, S. Haigh, C. Hardacre, M. Schröder, S. Yang, *J. Am. Chem. Soc.* **2021**, *143*, 10977–10985.
[31] M. SK, M. Grzywa, D. Volkmer, S. Biswas, *J. Solid State Chem.* **2015**, *232*, 221–227.
[32] H. Wang, X. Dong, J. Lin, S. Teat, S. Jensen, J. Cure, E. Alexandrov, Q. Xia, K. Tan, Q. Wang, D. Olson, D. Proserpio, Y. Chabal, T. Thonhauser, J. Sun, Y. Han, J. Li, *Nat. Commun.* **2018**, *9*, 1745.
[33] Y. Yan, A. O'Connor, G. Kanthasamy, G. Atkinson, D. Allan, A. Blake, M. Schröder, *J. Am. Chem. Soc.* **2018**, *140*, 3952–3958.
[34] N. Tannert, Y. Sun, E. Hasturk, S. Niebing, C. Janiak, *Z. Anorg. Allg. Chem.* **2021**, *647*, 1124–1130.
[35] L. Myers, M. Prausnitz, *AIChE J.* **1965**, *11*, 121–127.
[36] S. Seddiek, M. Elgohary, *Int. J. Nav. Archit. Ocean Eng.* **2014**, *6*, 737–748.
[37] S. Narang, V. Kartha, N. Patel, *Physica C* **1992**, *204*, 8–14.
[38] V. Hernández, J. Ramírez, J. Casado, J. López-Navarrete, *J. Phys. Chem.* **1996**, *100*, 2907–2914.
[39] D. Zheng, Y. An, Z. Li, J. Wu, *Angew. Chem. Int. Ed.* **2014**, *53*, 2451–2454; *Angew. Chem.* **2014**, *126*, 2483–2486.
[40] J. Li, Z. Zhou, X. Han, X. Zhang, Y. Yan, W. Li, G. Smith, Y. Cheng, L. McPherson, S. Teat, M. Frogley, S. Rudic, A. Ramirez-Cuesta, A. Blake, J. Sun, M. Schröder, S. Yang, *J. Am. Chem. Soc.* **2020**, *142*, 19189–19197.

Manuscript received: May 17, 2022
Accepted manuscript online: June 23, 2022
Version of record online: July 25, 2022